Lidar remote sensing of laser-induced incandescence on light absorbing particles in the atmosphere

Alain Miffre, Christophe Anselmo, Sylvain Geffroy, Emeric Fréjafon, Patrick Rairoux

Lidar remote sensing of laser-induced incandescence on light absorbing particles in the atmosphere

Alain Miffre,[1] Christophe Anselmo,[1] Sylvain Geffroy,[2] Emeric Fréjafon[3] and Patrick Rairoux[1,*]

[1]*Institut Lumière Matière, UMR5306 Université Lyon 1-CNRS, Université de Lyon 69622 Villeurbanne cedex, France*
[2]*Thales Communication and Security, 4 avenue des Louvresses, 92230 Gennevilliers, France*
[3]*Institut National de l'Environnement Industriel et des Risques, F-60550 Verneuil-en-Halatte, France*
[*]*patrick.rairoux@univ-lyon1.fr*

Abstract: Carbon aerosol is now recognized as a major uncertainty on climate change and public health, and specific instruments are required to address the time and space evolution of this aerosol, which efficiently absorbs light. In this paper, we report an experiment, based on coupling lidar remote sensing with Laser-Induced-Incandescence (LII), which allows, in agreement with Planck's law, to retrieve the vertical profile of very low thermal radiation emitted by light-absorbing particles in an urban atmosphere over several hundred meters altitude. Accordingly, we set the LII-lidar formalism and equation and addressed the main features of LII-lidar in the atmosphere by numerically simulating the LII-lidar signal. We believe atmospheric LII-lidar to be a promising tool for radiative transfer, especially when combined with elastic backscattering lidar, as it may then allow a remote partitioning between strong/less light absorbing carbon aerosols.

OCIS codes: (010.3640) Lidar; (290.6815) Thermal emission; (010.1100) Aerosol detection; (290.1350) Backscattering.

References and links

1. IPCC, *Climate Change 2013: The Physical Science Basis. Working Group I Contribution to the Fifth Assessment Report of the Intergovernmental Panel on Climate Change* (Cambridge University Press, (2013).
2. G. David, B. Thomas, T. Nousiainen, A. Miffre, and P. Rairoux, "Retrieving simulated volcanic, desert dust, and sea-salt particle properties from two / three-component particle mixtures using UV-VIS polarization Lidar and T-matrix," Atmos. Chem. Phys. **13**(14), 6757–6776 (2013).
3. A. Ansmann, A. Petzold, K. Kandler, I. Tegen, M. Wendisch, D. Muller, B. Weinzerl, T. Muller, and J. Heintzenberg, "Saharan Mineral Dust Experiments SAMUM-1 and SAMUM-2: what have we learned?" Tellus B Chem. Phys. Meterol. **63**(4), 403–429 (2011).
4. P. Stier, J. H. Seinfeld, S. Kinne, and O. Boucher, "Aerosol absorption and radiative forcing," Atmos. Chem. Phys. **7**(19), 5237–5261 (2007).
5. J. Löndhal, E. Switelicki, E. Lindgren, and S. Loft, "Aerosol exposure versus aerosol cooling of climate: what is the optimal reduction strategy for human health?" Atmos. Chem. Phys. **10**(19), 9441–9449 (2010).
6. T. Bond and R. Bergstrom, "Light absorption by carbonaceous particles: an investigative review," Aerosol Sci. Technol. **40**(1), 27–67 (2006).
7. M. Francis, J. B. Renard, E. Hadamcik, B. Couté, B. Gaubicher, and M. Jeannot, "New studies on scattering properties of different kinds of soot and carbon-black," J. Quant.Spectrosc.Radiat.Trans. **112**, 1766–1775 (2011).
8. M. Laborde, M. Schnaiter, C. Linke, H. Saathoff, K.-H. Naumann, O. Möhler, S. Berlenz, U. Wagner, J. W. Taylor, D. Liu, M. Flynn, J. D. Allan, H. Coe, K. Heimerl, F. Dahlkötter, B. Weinzierl, A. G. Wollny, M. Zanatta, J. Cozic, P. Laj, R. Hitzenberger, J. P. Schwarz, and M. Gysel, "Single Particle Soot Photometer intercomparison at the AIDA chamber," Atmos. Meas. Tech. **5**(12), 3077–3097 (2012).
9. S. Baidar, H. Oetjen, S. Coburn, B. Dix, I. Ortega, R. Sinreich, and R. Volkamer: "The CU Airborne MAX-DOAS Instrument: Vertical Profiling of Aerosol Extinction and Trace Gases", A.M.T. Atm. Meas. Tech. **6**, 719–719–739, (2013).
10. B. Thomas, G. David, C. Anselmo, J.-P. Cariou, A. Miffre, and P. Rairoux, "Remote sensing of atmospheric gases with optical correlation spectroscopy and Lidar: first experimental results on water vapor profile measurements," Appl. Phys. B **113**(2), 265–275 (2013).

#226547 - $15.00 USD Received 7 Nov 2014; revised 8 Jan 2015; accepted 9 Jan 2015; published 28 Jan 2015

11. G. David, A. Miffre, B. Thomas, and P. Rairoux, "Sensitive and accurate dual-wavelength UV-VIS polarization detector for optical remote sensing of tropospheric aerosols," Appl. Phys. B **108**(1), 197–216 (2012).
12. G. David, B. Thomas, Y. Dupart, B. D'Anna, C. George, A. Miffre, and P. Rairoux, "UV polarization lidar for remote sensing new particles formation in the atmosphere," Opt. Express **22**(S3 Suppl 3), A1009–A1022 (2014).
13. M. Schnaiter, H. Horvath, O. Möhler, K.-H. Naumann, H. Saathoff, and O. W. Schöck, "UV-VIS-NIR spectral optical properties of soot and soot-containing aerosols," J. Aerosol Sci. **34**(10), 1421–1444 (2003).
14. M. Stephens, N. Turner, and J. Sandberg, "Particle identification by laser-induced incandescence in a solid-state laser cavity," Appl. Opt. **42**(19), 3726–3736 (2003).
15. H. A. Michelsen, "Laser-induced incandescence of flame-generated soot on a picosecond time scale," Appl. Phys. B **83**(3), 443–448 (2006).
16. C. Schulz, B. F. Kock, M. Hofmann, H. Michelsen, S. Will, B. Bougie, R. Suntz, and G. Smallwood, "Laser-induced incandescence: recent trends and current questions," Appl. Phys. B **83**(3), 333–354 (2006).
17. R. J. Santoro and R. Shaddix, "Laser-Induced Incandescence", in Applied Combustion Diagnostics, Taylor and Francis, New York. p. 252–286, (2002).
18. H. Bladh, P. E. Bengtsson, J. Delhay, Y. Bouvier, E. Therssen, and P. Desgroux, "Experimental and theoretical comparison of spatially-resolved laser-induced-incandescence signals of soot in backward and right-angle configuration," Appl. Phys. B **83**(3), 423–433 (2006).
19. B. Kaldvee, C. Brackmann, M. Aldén, and J. Bood, "LII-lidar: range-resolved backward picosecond laser-induced incandescence," Appl. Phys. B **115**(1), 111–121 (2014).
20. R. M. Measures, "Laser Remote Sensing: Fundamentals and Applications" Krieger publishing company, Malabar, Florida, USA, (1992).
21. D. R. Snelling, F. Liu, G. Smallwood, and O. Gülder, "Determination of the soot absorption function and thermal accommodation coefficient using low-fluence LII in a laminar coflow ethylene diffusion frame," Combust. Flame **136**(1-2), 180–190 (2004).
22. F. Liu, K. J. Daun, D. R. Snelling, and G. J. Smallwood, "Heat conduction from a spherical nano-particle: status of modeling heat conduction in laser-incandescence," Appl. Phys. B **83**(3), 355–382 (2006).
23. C. M. Sorensen, J. Cai, and N. Lu, "Light-scattering measurements of monomer size, monomers per aggregate, and fractal dimension for soot aggregates in flames," Appl. Opt. **31**(30), 6547–6557 (1992).
24. J. Yon, F. Liu, A. Bescond, C. Caumont-Prim, C. Rozé, F. X. Ouf, and A. Coppalle, "Effects of multiple scattering on radiative properties of soot fractal aggregates," J. Quant.Spectrosc.Radiat.Trans. **133**, 374–381 (2014).
25. M. Mishchenko, L. Liu, and D. W. Mackowski, "T-matrix modeling of linear depolarization by morphologically-complex soot and soot-containing particles," J. Quant.Spectrosc.Radiat.Trans. **123**, 135–144 (2013).
26. M. Kahnert, T. Nousiainen, H. Lindqvist, and M. Ebert, "Optical properties of light absorbing carbon aggregates mixed with sulphate: assessment of different model geometries for climate forcing calculations," Opt. Express **20**(9), 10042–10058 (2012).
27. H. Bladh, J. Johnsson, J. Rissler, H. Abdulhamid, N. E. Olofsson, M. Sanati, J. Pagels, and P. E. Bengtsson, "Influence of soot particle aggregation on time-resolved laser-inudced incandescence signals," Appl. Phys. B **104**(2), 331–341 (2011).
28. A. Miffre, M. Abou Chacra, S. Geffroy, P. Rairoux, L. Soulhac, R. J. Perkins, and E. Fréjafon, "Aerosol load study in urban area by Lidar and numerical model," Atmos. Environ. **44**(9), 1152–1161 (2010).

1. Introduction

As underlined by the latest IPCC report [1], atmospheric aerosols are nowadays recognized as a major uncertainty on climate change and global warming. This uncertainty originates from the complexity of atmospheric aerosols, which present a wide range of sizes, shapes and chemical composition, and exhibit a generally complex vertical layering, especially in the low troposphere where complex mixtures usually occur. Several laboratory and field experiments [2,3] have hence been performed to study this complex vertical layering for volcanic ash, desert dust, or sea-salt particles in the troposphere. Among all atmospheric aerosols, the carbon aerosol plays a key role, black carbon being the second contributor to global warming after CO_2 [1] as a major absorber of solar radiation [4]. Additionally, the carbon aerosol has a strong impact on human health, especially in urban polluted areas, as being carcinogenic [5]. In the literature, the terminology related to the carbon aerosol is not straightforward, and involves all possible chemical forms of carbon, such as soot particles, carbonaceous particles, biomass burning, or secondary organic aerosols, to quote only a few. Recent reviews attempted to clarify the meaning of this terminology in regards to the measurement and characterization techniques [6–8]. However, there is still a need for determining the spatial and temporal distribution of the carbon aerosol in the atmosphere, especially in urban polluted areas, where it strongly impacts human health and global warming, sometimes during long lifetimes, as for black carbon. This task is essential for radiative forcing, to better understand the involved chemistry, as well as to develop carbon reduction emission strategies.

#226547 - $15.00 USD Received 7 Nov 2014; revised 8 Jan 2015; accepted 9 Jan 2015; published 28 Jan 2015

Basically, the interaction of light with atmospheric aerosols is described by light absorption, elastic / inelastic light scattering, and emission of light by Planck thermal radiation. As enhanced by LII-scientists, the LII-signal non linearly depends on the laser fluence, mainly because it strongly depends on the particle temperature (to the power of 5). Light backscattering and absorption are involved in the light detection and ranging technique (lidar), which provides the spatial and temporal distribution of particles backscattering from a remote place. Recent advances in this field concern both atmospheric molecules [9, 10] and aerosols up to three-component particle mixtures involving volcanic ash, desert dust, sea-salt or sulfate particles [2] with increased sensitivities [11], allowing henceforth even range-resolved lidar remote detection of new particles formation events [12]. However, to our knowledge, no lidar methodology exists that would allow a range-resolved specific detection of the strong light-absorbing carbon aerosol in the atmosphere over several hundreds of meters. In the literature, the light absorption properties of the carbon aerosol have been addressed in laboratory measurements on soot particles [13]. In general, absorption of light by the carbon aerosol results in a sharp increase of its temperature and the subsequent light emission by Planck thermal radiation, or incandescence, is size and shape particle dependent. Hence, new instruments have emerged such as the Single Particle Soot Photometer to perform measurements of the refractory black carbon mass [14]. This light-induced-incandescence (LII) technique is very efficient with nanosecond pulsed laser light allowing the electromagnetic radiation to efficiently interact with the carbon aerosol at the plasma frequency. At shorter laser pulse duration, two photons fluorescence of the particles may initiate perturbations on the LII signal [15]. A nice review on the LII-technique can be found in the literature [16, 17]. In particular, the energy balance and mass equations describing the interaction of light with the carbon aerosol are there numerically solved.

In this paper, we performed a field experiment, based on coupling the lidar and LII-techniques, to retrieve a range-resolved profile of LII-thermal radiation in an urban atmosphere over several hundreds of meters, which is new. We hence specifically detect atmospheric aerosols that strongly absorb light in the visible (VIS) and near-infrared (NIR) spectral ranges, hereafter designated by the terminology of Light Absorbing Particles (LAP). In the literature, backward-LII has been observed only in laboratory experiments [18, 19], the latter authors describing laboratory range-resolved observation of soot emissions from two gas burners up to a four meters distance. Hence, this work is far from the lidar methodology applied to the observation of the atmosphere over several hundreds of meters. Nevertheless, these laboratory studies show the ability of LII to achieve a range-resolved qualitative observation of soot volume fraction. Our paper is organized as follows. In Section 2, we develop the atmospheric LII-lidar formalism, suitable for range-resolved observations of LII-radiation in the atmosphere. Starting from Kirchhoff's law, we establish the LII-lidar equation by taking into account the LAP cooling time, following the LAP heating by laser-light absorption. The lidar volume incandescence coefficient β_{LII} is introduced, in analogy with the volume backscattering/fluorescence coefficients [20]. To address the main features of atmospheric LII-lidar, a numerical simulation of the LII-lidar signal is then performed as a function of the atmospheric LAP content and of the lidar laser characteristics. To operate the LII-lidar methodology in the atmosphere, two LII-lidar detector configurations are proposed in Section 3: one for spectrally-resolved measurements over a range altitude interval, one for retrieving range-resolved vertical profiles of LII in the atmosphere at a single wavelength. In Section 4, these two LII-lidar detectors are operated in an urban atmosphere (Lyon, France) over several hundreds of meters to address LAP in this atmosphere. Detecting the LII-radiation in the atmosphere is challenging, for its intensity is about 100 times lower than that of Raman vibrational sidebands. Using the spectrally-resolved LII-lidar configuration allows identifying the LII-radiation, by fitting the recorded spectrum with Planck's distribution, as a clear signature of LII. Moreover, by initiating LII in the IR spectral range, we removed the spectrum from Raman vibrational sidebands allowing accurate measurements of the LII-radiation. By operating the LII-lidar detector at a single wavelength, we provide the first LII-lidar vertical profile in an urban atmosphere. A discussion is then proposed to interpret the

#226547 - $15.00 USD Received 7 Nov 2014; revised 8 Jan 2015; accepted 9 Jan 2015; published 28 Jan 2015

observed LII-lidar vertical profile, by relying on Section 2 formalism and numerical simulation, in complement with the atmospheric vertical layering, provided by the recorded elastic backscattering profile. The paper ends with a conclusion and proposes outlooks on the combination of the atmospheric LII-lidar methodology with the backscattering lidar methodology.

2. Atmospheric LII-lidar formalism

In this section, we set the atmospheric LII-lidar formalism, obtained by combining the lidar and LII techniques in the atmosphere. The atmospheric LII-lidar equation is provided by taking into account the LAP-cooling time. Then, a numerical simulation is performed to address the main features of LII-lidar in the atmosphere over several hundred of meters.

2.1 The atmospheric LII-lidar equation

Let us consider a lidar laser source emitting a pulse of energy E_L at a wavelength λ_L during a time τ_L. As for the lidar technique [20], the atmospheric LII-lidar methodology consists in measuring the time-of-flight $t = 2R/c$ taken by the leading edge of a laser pulse to propagate back (and forth) from the atmosphere over a range R, the range resolution $\delta R = c\tau_L/2$ being defined by the laser pulse duration τ_L. As for the LII-technique, absorption of electromagnetic energy results in a LAP-temperature increase up to a peak value T_{max}, beyond which LAP cool down to the ambient temperature T_a through incandescence (LII), thermal conduction with the background ambient gas, and evaporation by sublimation. In the LAP-frame, laser absorption begins at the time $t^* = 0$ where the leading edge of the laser pulse encounters the LAP-particle and occurs up to a time close to the laser pulse duration τ_L. The LAP-peak temperature T_{max} can then be evaluated from the energy balance equation by assuming that cooling processes are negligible during the laser pulse absorption [21]. When the laser beam propagates into the atmosphere over several hundreds of meters as in the atmospheric LII-lidar methodology, when increasing the range R, the laser energy spreads over a larger surface because of the laser beam divergence θ_L. Hence, as the range R increases, the LAP-peak temperature T_{max} decreases, which in turn reduces the emitted LII-radiation, as quantitatively described in Section 2.2. For $t^* \geq \tau_L$, below the LAP-sublimation point, LAP cool down to the ambient temperature T_a by LII and thermal conduction [22] which occur during a characteristic time τ, which depends on the LAP-radius a (for non-spherical LAP, a volume equivalent radius can be defined). Hence, in the most general case, a numerical simulation is needed to get the time evolution of the LAP-temperature T_p.We now focus on the collection of the LII-thermal radiation emitted by LAP within the lidar geometry to derive the LII-lidar equation. We start from the expression of the LII-spectral intensity emitted by a spherical LAP, i.e. $I_{LII}(\lambda,a) = \varepsilon_\lambda B_\lambda(T_p) \times 4\pi a^2$, where λ is the wavelength of the LII-radiation, ε_λ is the LAP-spectral emissivity, and $B_\lambda(T_p)$ is the Planck blackbody spectral radiance at temperature T_p. Following Kirchhoff's law, the spectral emissivity ε_λ equals the spectral absorptivity Q_{abs}. Hence, at a range R from the LAP-target, the spectral intensity reaching the surface A_0 of a lidar telescope is given by:

$$I_{LII}(\lambda,a,R) = I_{LII}(\lambda,a)\times\frac{A_0}{4\pi R^2} = 4\sigma_{abs}B_\lambda(T_p)\times\frac{A_0}{4\pi R^2} \quad (1)$$

Equation (1) is valid for monodisperse LAP having $\sigma_{abs} = Q_{abs} \times \pi a^2$ for absorption cross-section. Since the characteristic cooling time $\tau(a)$ is generally higher than τ_L (τ is typically equal to 1 µs while τ_L is 10 ns), the LAP size distribution must be taken into account in the atmospheric LII-lidar methodology for precise retrievals of range-resolved LII-profiles. Hence, at a range R from the laser-irradiated LAP-target, the collected LII-power emitted at wavelength λ is the integral of the LII-radiation emitted by individual LAP over the LAP size distribution:

$$P_{LII}(\lambda,R) = \int_0^\infty da\, n_p(a,R)A_L(R)c\tau_L I_{LII}(\lambda,a,R) \quad (2)$$

#226547 - $15.00 USD Received 7 Nov 2014; revised 8 Jan 2015; accepted 9 Jan 2015; published 28 Jan 2015

where $n_p(a, R)$ is the LAP number density and $A_L(R)\cdot c\tau_L$ is the laser-illuminated volume at range R during the laser pulse duration τ_L, when assuming a spatially uniform laser pulse intensity at range R ($A_L(R) = \pi R^2\theta_L^2$ is the laser-illuminated area at range R). By combining Eqs. (1) and (2), we get:

$$P_{LII}(\lambda, R) = K_0 \int_0^\infty da\, n_p(a,R)\sigma_{abs}(a)B_\lambda(T_p) \quad (3)$$

where $K_0 = A_0\theta_L^2 c\tau_L$ is a constant for a given lidar laser source and telescope geometry. Equation (3) must be corrected to account for the characteristic cooling time τ. Hence, the incandescence induced by the leading edge of the laser pulse at range R and propagating towards the detector will be reinforced by the incandescence emanating from the target medium at range R' (R' < R), having been exposed to laser radiation for a period t' = 2(R-R')/c. In other words, due to the cooling time τ, the LII-lidar signal detected at time t = 2R/c not only originates from the LII-radiation emitted by LAP-particles located at range R, but also from LAP-particles located at range R', which have cooled down for a time t' = 2(R-R')/c. Hence, the LAP-temperature to be considered in Eq. (3) is $T_p(a,t' = 2(R-R')/c) = T_p(a,R-R')$ and the contribution of every possible range R', from zero up to R, must then be taken into account to get the atmospheric LII-lidar equation, providing the LII-lidar signal $S_{LII\text{-}lidar}$:

$$S_{LII-lidar}(\lambda, R) = \frac{S_0}{4\pi}\int_0^R dR' \int_0^\infty da\, n_p(a,R')\sigma_{abs}(a)T(\lambda,R')B_\lambda[\lambda, T_p(a,R-R')] \quad (4)$$

where $T(\lambda, R')$ is the transmission of the atmosphere which accounts for the extinction of LII-radiation from the emitting volume to the lidar detector. $S_0 = 4\pi K_0$ and to ease the reading, we omitted the λ_L-dependency of $S_{LII\text{-}lidar}$. The atmospheric LII-lidar Eq. (4) can be simplified by introducing a lidar volume incandescence coefficient $\beta_{LII}(\lambda_L,R)$ in analogy with the backscattering/fluorescence lidar [20]:

$$\beta_{LII}(\lambda_L, R) = \frac{1}{4\pi}\int_0^\infty da\, n_p(a,R)\,\sigma_{abs}(\lambda_L, a) \quad (5)$$

As for the volume lidar backscattering coefficient, the volume incandescence coefficient β_{LII} expresses in $m^{-1}.sr^{-1}$, but it is null for non-LAP particles, which cannot experience LII-lidar. For particles in the Rayleigh limit (size parameters $x = 2\pi a/\lambda_L << 1$), such as soot particles, β_{LII} is proportional to the size-averaged soot volume fraction $f_v(R)$, i.e. $\beta_{LII}(\lambda_L, R) = 6E(m)f_v(R)/\lambda_L$ by introducing $E(m) = Im((m^2-1)/(m^2+2))$ for a m-complex refractive index of soot particles. Hence, the β_{LII}-coefficient may provide range-resolved size-averaged soot-volume fractions vertical profiles if E(m) is known. When introducing β_{LII} in Eq. (5), the LII-lidar equation takes the simpler following form:

$$S_{LII-lidar}(\lambda, R) = S_0\beta_{LII}(\lambda_L)T(\lambda) \otimes_R B_\lambda[\lambda, T_p] \quad (6)$$

where $\otimes_R$ is the mathematical sign for the convolution product performed over range R' from zero to R and $T_p(a, R)$ has been approximated by its size-averaged value $T_p(a_0, R)$ at the mean LAP-particles radius a_0. Interestingly, in contrary to the backscattering lidar equation, the LII-lidar equation does not exhibit any $1/R^2$-dependency with range R, due to the simplification of the collection solid angle with the laser-illuminated volume, itself proportional to R^2. However, the LAP-peak temperature, which decreases with R, reduces the accessible range of the LII-lidar set-up, as detailed in Section 2.2. Equations (4), (6) are valid for a monochromatic LII-lidar detector, at ranges where the lidar geometrical overlap function becomes equal to unity. In general, the detector time resolution is below the characteristic cooling time τ so that the convolution product reduces to only a few ranges. The spectral dependence of the LII-lidar spectrum can be adjusted with Planck's distribution to determine

#226547 - $15.00 USD Received 7 Nov 2014; revised 8 Jan 2015; accepted 9 Jan 2015; published 28 Jan 2015

the LAP-temperature, as detailed in Section 4.1. In complement, range-resolved lidar vertical profiles of LII-radiation emitted by LAP in the atmosphere should follow Eq. (4), as discussed in Section 4.2.

2.2 Atmospheric LII-lidar numerical simulation

To address the main features of atmospheric LII-lidar over several hundreds of meters, we numerically simulated the LII-lidar Eq. (4). As a first step, we evaluated the LAP-peak temperature T_{max} at a range R from the lidar laser source. By solving the energy balance equation in the Rayleigh limit, we get the following expression for T_{max}, by assuming that no cooling occurs during the laser pulse duration:

$$T_{\max}(R) = T_a + \frac{6\pi E(m)}{\lambda_L \rho c_p} \frac{E_L T(\lambda_L, R)}{\pi (R^2 \theta_L{}^2 + d_0^2)} \tag{7}$$

where d_0 is the beam diameter at range R = 0, while ρ and c_p respectively refer to the LAP-density and heat mass capacity. As displayed in Fig. 1(a), the LAP-peak temperature decreases with range R, since the laser beam divergence θ_L spreads the laser energy over a larger surface. Therefore, to operate the atmospheric LII-lidar methodology over several hundreds of meters, the laser beam divergence must be sufficiently low.

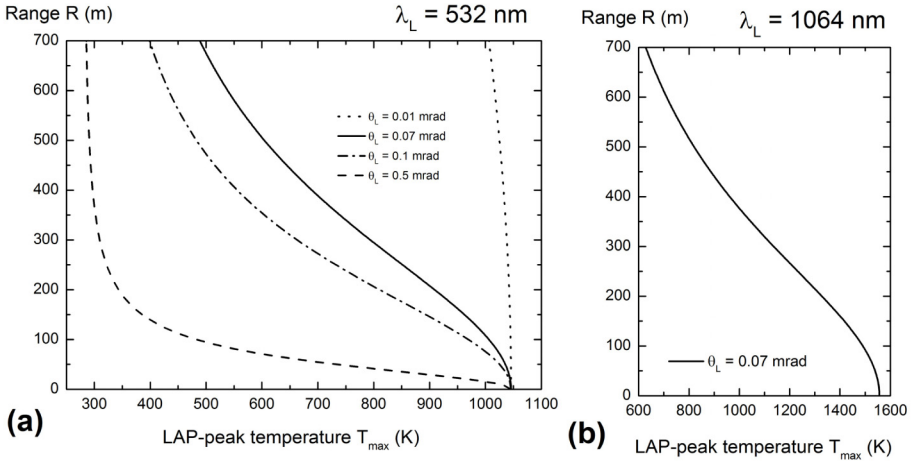

Fig. 1. (a) LAP-peak temperature T_{max} at a range R from the lidar laser source computed from Eq. (7) at λ_L = 532 nm for four laser beam divergence: θ_L = 0.01 mrad (dotted line), θ_L = 0.07 mrad (full line), θ_L = 0.1 mrad (dash-dotted line), θ_L = 0.5 mrad (dashed line), for the following set of laser parameters (E_L = 150 mJ, d_0 = 30 mm). LAP are assumed to be Diesel soot particles (m = 1.49 + 0.67i, ρ = 1700 kg.m^{-3}, c_p = 1900 J.kg^{-1}.K^{-1}), as published by Schnaiter et al. [13]. The atmospheric transmission T is equal to one and T_a = 280 K. (b) Same as panel (a) for λ_L = 1064 nm and E_L = 500 mJ, to be used in Section 4.2.

We then numerically simulated the LII-lidar Eq. (4) for a flat-top LAP vertical profile, used as input atmosphere. For computing the LAP absorption cross-section σ_{abs}, we applied the Rayleigh-Gans theory [23]. This light-absorption model can be improved, as recently proposed by Yon et al. [24], Mishchenko et al. [25] or Kahnert et al. [26], but this task is beyond the scope of this paper, devoted to the remote observation of LII in the atmosphere. The time-evolution of the LAP-temperature can be obtained by solving the energy balance equation [22]. When thermal conduction is the main cooling process, T_p follows an exponential decay law, i.e. $T_p(a,t) = T_a + (T_{max} - T_a) \times \exp(-t/\tau(a))$. In the most general case, the expression of $T_p(a,t)$ is no longer analytical and a numerical simulation must be performed to get the expression of $T_p(a,t)$. For evaluating the cooling time τ in the low troposphere, we noted that thermal conduction with the background ambient air must be described in the

#226547 - $15.00 USD Received 7 Nov 2014; revised 8 Jan 2015; accepted 9 Jan 2015; published 28 Jan 2015

transition regime, since the ambient air pressure corresponds to Knudsen numbers in the range of a few units, intermediate between the free-molecular and continuum regimes. We hence combined Eqs. (32) to (35) from Liu et al. [22] with the energy balance equation to retrieve the LAP-characteristic cooling time τ, by assuming that no laser absorption occurs at times above τ_L. Figure 2 provides the retrieved range-resolved LII-lidar signal for a flat-top LAP profile composed of Diesel soot particles [13] (constant value up to R_0 = 300 meters, null value at above altitudes). In this case, below R_0, the range dependence of the LII-lidar signal is determined by the range dependence of the LAP-temperature contained in the Planck function B_λ. Hence, if the laser beam divergence was null, the retrieved LII-lidar profile would increase with range up to R_0, and at higher ranges, the LII-lidar signal would not be null but slowly decreasing with range R, as a consequence of the cooling time τ. This behavior is analogous to the charge of a capacitor submitted to a Heaviside step function. The laser beam divergence, which induces a decrease of T_{max} with range R, counterbalances this increase of $S_{LII\text{-}lidar}$ with range R so that a maximum occurs in the LII-lidar signal retrieved in Fig. 2. The strong dependence of the LII-lidar signal on the laser beam divergence originates from its nonlinear dependence with the laser fluence. Then, above this maximum, the LII-lidar signal decreases with time due to the cooling time τ. Hence, care should be taken when analyzing range-resolved LII-lidar vertical profiles, for the cooling time τ and the subsequent convolution product, as well as the $1/R^2$-decrease of T_{max} may lead to a very low LII-lidar signal, though the LAP-profile confirms the LAP-presence, with the same LAP-content as at lower altitudes. Hence, our numerical simulation shows that, even in the simple case of a step Heaviside LAP-profile, the relationship between the LII-lidar signal and the LAP-content is not straightforward.

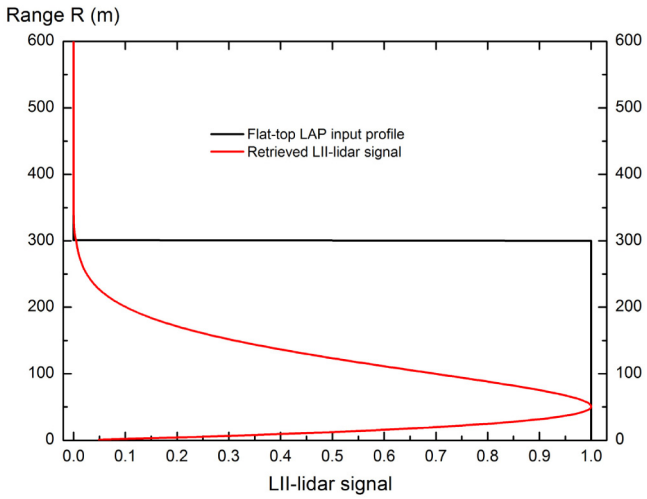

Fig. 2. Numerical simulation of the LII-lidar signal (red) for an input flat-top LAP profile (Heaviside step function up to R_0 = 300 meters, black). The laser characteristics are E_L = 500 mJ, λ_L = 1064 nm, θ_L = 0.07 mrad and d_0 = 30 mm. LAP are assumed to be Diesel soot particles (27 nm monomer size, 2.0 fractal dimension from [13]). The cooling time shaping the LII-lidar signal is 1 µs and the particles size distribution is also taken from [13]. The LII-radiation is detected at wavelength λ = 633 nm. To ease the reading, the LII-lidar signal has been normalized to its maximal value.

3. Atmospheric LII-lidar experimental set-up

In this section, the LII-lidar experimental set-up is presented. Two experimental detector configurations are proposed, allowing either spectrally-resolved LII-lidar measurements over a range interval, or range-resolved LII-lidar measurements at a single detection wavelength (*1λ-LII-lidar)*. The latter configuration is coupled with an elastic backscattering lidar,

#226547 - $15.00 USD Received 7 Nov 2014; revised 8 Jan 2015; accepted 9 Jan 2015; published 28 Jan 2015

sensitive to all atmospheric aerosols, either refractory, which may incandesce, or not. Figure 3 presents the achieved experimental set-up. The lidar laser source is a (doubled) Nd:YAG laser source, emitting 10 ns-laser pulses of energy E_L = 150 mJ in the VIS spectral range at wavelength λ_L = 532 nm (E_L = 500 mJ in the IR spectral range at λ_L = 1064 nm). The initial beam diameter at range R = 0 is d_0 = 30 mm after a 10x-beam expander, used to fix the laser beam divergence to θ_L = 0.07 mrad. The LAP LII-thermal radiation and the backscattered radiation – either elastic or inelastic –, are collected with a 200 mm diameter f/3-Newtonian telescope before entering our home-built LII-lidar detector, whose configurations are now described in details.

3.1 Spectrally-resolved LII-lidar detector

Spectrally-resolved measurements are used to identify the LII-radiation by fitting them with the Planck's spectrum. As shown in Fig. 3, in this configuration, the laser source is operated at λ_L = 532 nm and the collected electromagnetic radiation is first removed from its elastic contribution with a very efficient Notch filter (super holographic, optical density of 8, 0.2 nm bandwidth). Then, the remaining LII and inelastic backscattering radiations are spectrally-resolved with a 250 mm focal length Imaging Czerny-Turner Spectrometer, coupled to an Andor's fast-gated Gen 3 Intensified CCD camera.

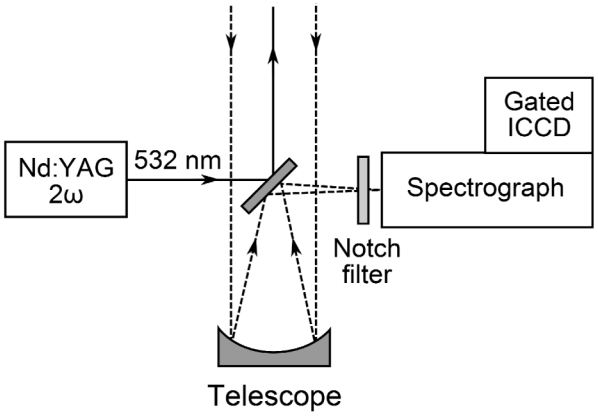

Fig. 3. Experimental set-up for spectrally-resolved atmospheric LII-lidar measurements. After laser pulse excitation at λ_L = 532 nm wavelength, the elastic/non-elastic backscattering radiations and the LII-radiation are collected with a f/3 Newtonian telescope. The 532 nm-Notch filter aims at removing the elastic contribution from the atmosphere and from the adjacent lidar laser source. The 250 mm focal length Imaging Czerny-Turner Spectrometer coupled with the ICDD gated camera allows time (range) and spectrally-resolved LII-lidar measurements, in the VIS and near IR spectral ranges.

The ICCD camera (1024 x 1024 pixels resolution) runs in the photon-counting mode, is equipped with thermoelectric cooling facilities (down to 210 K) and low noise electronics, allowing low dark counts (100 $e^-.s^{-1}$ per frame of 1024 x 1024 pixels) over a very high 16 bits dynamical range. A calibrated spectral light source (Ocean Optics) was placed in front of the telescope to spectrally calibrate our LII-lidar detector. The ICDD camera and the gated obturator were chosen for their sensitivity in the VIS and NIR spectral ranges. The LII-lidar signal is hence representative of a dedicated range of the atmosphere, and moreover, the range interval over which such an average is performed can be set by the ICCD trigger facility (the ICCD timegate is 2 μs). Hence, the LII-Lidar thermal radiation is simultaneously time (range) and spectrally-resolved.

3.2 Range-resolved LII-lidar detector at a single wavelength (1λ-LII lidar detector)

Range-resolved LII-lidar measurements at a single detection wavelength are used to provide vertical profiles of LII-radiation in the atmosphere. As shown in Fig. 4, the 1λ-LII-lidar

#226547 - $15.00 USD Received 7 Nov 2014; revised 8 Jan 2015; accepted 9 Jan 2015; published 28 Jan 2015

detector allows LII-lidar measurements at a single wavelength (1λ-LII-Lidar) as well as lidar elastic backscattering measurements at λ_L = 532 nm, both radiations being spectrally discriminated by a dichroic beam-splitter. The elastic backscattering channel is used to address the vertical layering of atmospheric aerosols and was acquired alternatively with the LII-radiation during 100 s at a small laser energy (E_L = 5 mJ), in contrary to the LII-radiation, acquired with a high laser energy (E_L = 500 mJ) for 30 minutes, chosen as reasonable for observations in the atmosphere. The LII-radiation is excited in the IR spectral range (λ_L = 1064 nm) to avoid fluorescence from PAH-molecules, which are often present in urban atmospheres [15], and may influence the detected signal, even at high atmospheric quenching rates. The elastic backscattering channel has been detailed in [11] and is mainly composed of a 0.5 nm-interference filter (IF532) and a VIS-sensitive photomultiplier (PM532). The LII-channel is composed of a dual super Notch filter at wavelengths 532 and 1064 nm, combined with a 1 nm-interference filter centered at λ = 633 nm (IF633) to discriminate the LII-lidar radiation at 633 nm from other electromagnetic radiations, by a factor of 10^9. The λ = 633 nm choice for detecting the LII-radiation results from an interplay between the spectral sensitivity of the low-noise photomultiplier (PM633) and the intensity of the LII-radiation.

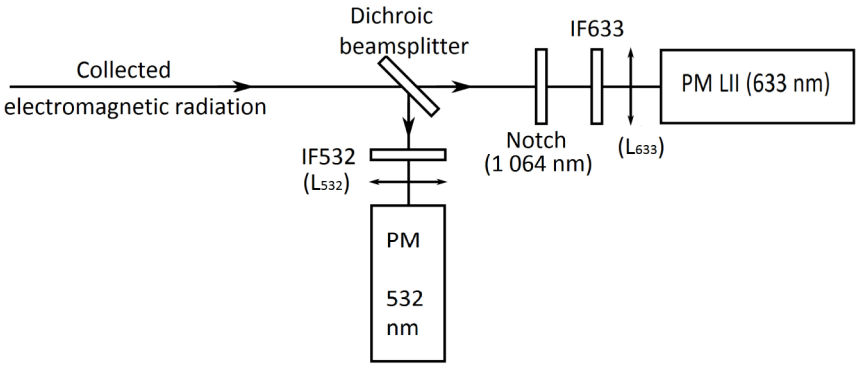

Fig. 4. Experimental set-up for range-resolved atmospheric LII-lidar measurements at a single detection wavelength (1λ-LII-lidar). The lidar laser source and telescope are identical to Fig. 3. Elastic backscattering is detected with the 532 nm-channel composed of an interference filter (IF532), a focusing lens (L532) and a photomultiplier (PM 532 nm). The LII-lidar radiation is discriminated from elastic backscattering with the dichroic beam-splitter and is detected at λ = 633 nm after laser excitation at λ_L = 1064 nm to avoid PAH fluorescence and remove the detected signal from its Raman inelastic contributions. The LII-channel is composed of a dual Notch filter (OD 8, 0.2 nm-bandwidth), an interference filter (IF633), a focusing lens (L633) and a PM (633 nm). The VIS and IR laser pulses are not simultaneously emitted to avoid wavelength cross-talks between the elastic (λ_L = λ = 532 nm) and the LII-channel (λ_L = 1064 nm, λ = 633 nm).

Moreover, by initiating LII in the IR spectral range then detecting the LII-radiation in the VIS spectral range, the LII-lidar signal is removed from its non-elastic Raman backscattering contributions due to atmospheric molecules such as nitrogen (N_2), oxygen (0_2) or water vapor (H_20). This down-conversion process ($\lambda_L > \lambda$) is key for precise observations of the LII-lidar signal, whose intensity is about 100 times lower than that of molecular Raman backscattering, as discussed in Section 4. Finally, due to the weakness of the LII-radiation, the 1λ-LII-Lidar signal has been recorded by operating the PM633 in the photon-counting mode during a 30 minutes acquisition time. For the LII-lidar signal (resp. the backscattering signal), the generated photoelectrons are recorded with a 250 MHz-12 bits Licel Transient Recorder (resp. 40 MHz). The range resolution is 22.5 meters after a 3-points (resp. 6-points) range averaging.

#226547 - $15.00 USD Received 7 Nov 2014; revised 8 Jan 2015; accepted 9 Jan 2015; published 28 Jan 2015

4. Results and discussion

In this section, we report on the first remote observation of LII-radiation in an urban atmosphere. We begin by performing spectrally-resolved LII-lidar measurements, before presenting an atmospheric LII-lidar vertical profile, achieved over several hundreds of meters.

4.1 Spectrally-resolved LII-lidar measurements in the troposphere

Figure 5 presents the spectrum of the atmospheric LII-lidar signal in the form of three successive expanded panels, labeled from (a) to (c), obtained with the experimental set-up presented in Fig. 3, by operating the ICCD gated camera in the Lyon troposphere for 30 minutes (18 000 lasers shots), over a range of 300 meters starting from the ground, during a moonless night. In Fig. 5(a), we clearly identify elastic and inelastic Raman atmospheric contributions, the former being efficiently reduced by the 532 nm-Notch filter. As expected, very close to the 532 nm-laser excitation wavelength, the acquired spectrum exhibits the rotational Stokes and Anti-Stokes Raman sidebands from atmospheric N_2 and O_2 while the vibrational Raman sidebands of O_2, N_2 and H_20 are located at higher wavelengths, 580, 607 and 660 nm respectively. The water vapor content over 300 meters altitude could then be retrieved, by calibrating our lidar set-up in regards to the meteorological parameters, but this task is far beyond the scope of this contribution dedicated to LII-lidar in the atmosphere. Interestingly, as to be seen in Fig. 5(b), which is a vertical 30 x-magnification of Fig. 5(a), for wavelengths above 700 nanometers, a very low signal increase could be recorded after detector noise subtraction, thanks to the performances of the ICDD camera (16 bits dynamical range, thermoelectric cooling facility, low noise electronics, low dark count). In contrary to elastic and inelastic backscattering, this signal is continuous and strongly increases in the red spectral part of the spectrum, up to the upper limit of 870 nm of the Gen 3 ICCD camera. By applying a peak-fit algorithm, we removed the molecular Raman scattering peaks from the spectrum to retrieve the Fig. 5(c) spectrum after vertical 2x-magnification. We are confident that Fig. 5(c)'s spectrum results from LII on laser-heated LAP particles for several reasons. Firstly, as shown in Fig. 5(c), this signal can be fitted with Planck's distribution, which is a clear signature of the LII-radiation emitted by LAP. We hence retrieve an atmospheric temperature T_p = 928 K, which represents the mean temperature of atmospheric particles over a range of 300 meters starting from the ground. To account for possible systematic errors induced by changes in atmospheric conditions during the 30 minutes acquisition time, we added 30%-confidence bands to Fig. 5(c), which corresponds to a 20 Kelvins uncertainty on T_p. Interestingly, the retrieved T_p-value is consistent with our numerical simulation of the LAP-peak temperature plotted in Fig. 1(a), for the 0.07 mrad laser divergence operated in our set-up. In the atmosphere, the sublimation of water and/or organic molecules could contribute to the attainable T_{max} and to the thermal conduction. In addition, by applying Wien's law, we checked that the observed signal could not originate from the Planck's radiation emitted by ambient air molecules (temperature T_a = 280 K): in the red part of the spectrum, LII by ambient molecules would lead to a signal which is 10^6 times lower than the observed one. Hence, and as we removed the recorded spectrum from its elastic and inelastic contributions, we are confident that the recorded signal displayed in Fig. 5(c) is the first experimental observation of LII on LAP in the troposphere from a remote place. Actually, to our knowledge, the state-of-the-art atmospheric science does not provide other physical process that may induce such a spectral increase. In Fig. 5(c), the intensity of the detected signal being about 100 times lower than a Raman vibrational signal, detecting the LII-lidar radiation in the low troposphere (up to 300 meters) is in the same range as detecting water vapor Raman sidebands at several kilometers altitude, which is feasible, during nighttime. In addition, the retrieved temperature being consistent with our numerical simulation, it indicates that LAP in the atmosphere optically behave like particles in the Rayleigh limit, with sizes in the tens of nanometer size range (bigger particles would have led to higher temperatures).

#226547 - $15.00 USD Received 7 Nov 2014; revised 8 Jan 2015; accepted 9 Jan 2015; published 28 Jan 2015

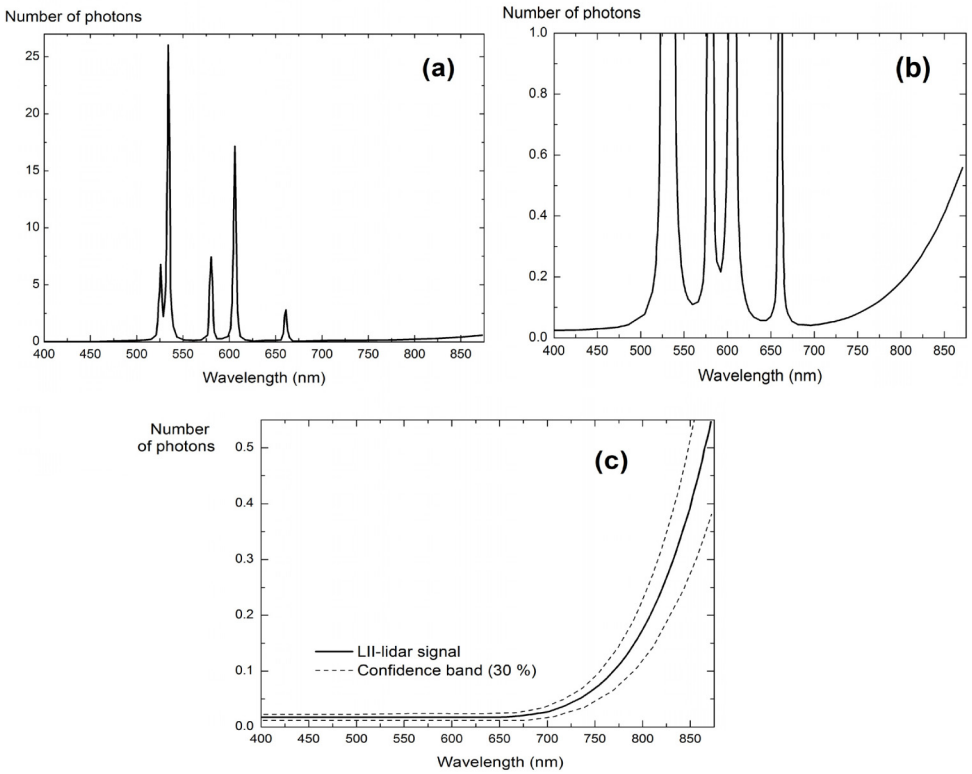

Fig. 5. Spectrum of the remotely detected atmospheric electromagnetic radiation recorded with the set-up presented in Fig. 3 above Lyon lidar station, over a range of 300 meters starting from the ground, during a moonless night. From panel (a) to (c), the spectrum is vertically magnified by a factor of 60. Once removed the panel (b)-Raman inelastic contributions, we get the panel (c) spectrum, obtained with a 30 minutes average photon counting over 18 000 laser shots, after a three-points smoothing (noise averaging). It can be adjusted with the Planck's distribution, as a clear LII-signature.

4.2 Vertical profile of LII-lidar radiation in the troposphere over several hundreds of meters

After acquiring the above LII-lidar spectrum, we operated the 1λ-LII-Lidar detector presented in Fig. 4 to measure the LII-vertical profile in the Lyon troposphere between 340 and 600 meters, as displayed in Fig. 6(a). These altitudes correspond to those for which the photon-counting detector provided reliable data for E_L = 500 mJ within our 30 minutes acquisition time. The LII-lidar signal decreases with altitude up to 600 meters, and between 450 and 600 meters, this decrease occurs at a smaller rate. To interpret this LII-Lidar signal, the formalism and the numerical simulation presented in Section 2 should be considered. As explained in Section 2.2, the relationship between the LII-lidar signal and the LAP-content is not straightforward. In particular, the volume incandescence coefficient β_{LII} is difficult to retrieve from the LII-Lidar signal, which is a convolution product of β_{LII} with the Planck thermal radiation, both depending on the altitude. However, the LII-lidar profile appears rather smooth, which is partly due to the convolution product in agreement with Section 2, in addition to our long acquisition time (30 minutes) at low altitudes and our three-point range averaging. Moreover, for our set of experimental parameters (λ_L = 1 064 nm, λ = 633 nm, E_L = 500 mJ, θ_L = 0.07 mrad), the decrease of the LII-lidar signal with range approximatively follows the decrease of the LAP-peak temperature with range plotted in Fig. 1(b).

#226547 - $15.00 USD Received 7 Nov 2014; revised 8 Jan 2015; accepted 9 Jan 2015; published 28 Jan 2015

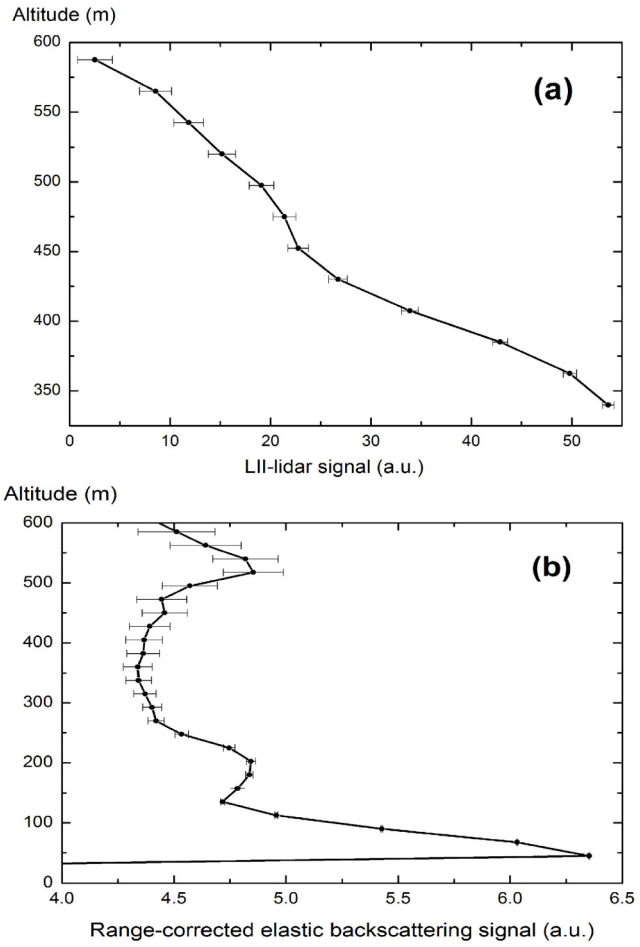

Fig. 6. Vertical profiles of LII-lidar signal (a) and elastic backscattering-lidar signal (b) acquired in the low troposphere of an urban city (Lyon, France) by using the 1λ-LII-lidar detector presented in Fig. 4. For the LII-radiation (a), the acquisition time is 30 minutes, λ_L = 1064 nm, λ = 633 nm, E_L = 500 mJ, θ_L = 0.07 mrad, leading to reliable photon-counting data between 325 and 600 meters. The laser fluence was limited by the available laser energy and emitting optics. The range-corrected lidar vertical profile (b) at λ_L = 532 nm is alternatively acquired during 100 s, with E_L = 5 mJ. The vertical resolution of both profiles is 22.5 m, as explained in Section 3.2.

The elastic backscattering Lidar signal at λ_L = 532 nm displayed in Fig. 6(b) also helps to interpret the LII-lidar vertical profile, by showing the vertical layering of atmospheric aerosols in the urban polluted atmosphere. In the Planetary Boundary Layer, these particles are well-mixed and distributed in three main layers in our case study: from ground level to 100 meters altitude, between 100 and 230 meters, then between 450 and 600 meters. Hence, if we consider that LAP are present in the Lyon‘s troposphere, LII should be observable in the different layers, since as shown in Section 4.1, the retrieved LAP-temperature is high enough to generate light in the spectral range where our PM and ICCD camera operate. Accordingly, the observed decrease of the LII-lidar signal with range (for altitudes up to 450 meters) may then result from the LII thermal decay of the laser-heated LAP present in the layers below 300 meters altitude. The observed decrease of the LII-lidar signal with altitude should then be explained with the model presented in Section 2.2, which we plotted in Fig. 2. Interestingly, the decrease of the LII-lidar signal with range can be used to roughly evaluate a characteristic cooling time τ = (800 ± 100) ns, close to that of our numerical simulation. This cooling time

#226547 - $15.00 USD Received 7 Nov 2014; revised 8 Jan 2015; accepted 9 Jan 2015; published 28 Jan 2015

may then possibly represent the radiative transfer decay by thermal conduction on LAP aggregates with sizes in the 100 nanometers range [27]. To confirm such a possible interpretation, co-located measurements of the LAP-content are needed. This task is beyond the scope of this paper and could not be performed at the time of the experiment with the available instruments (otherwise, no instrument provides range-resolved LAP-measurements as our LII-lidar does). Above 450 meters altitude, the LII-lidar signal may correspond to the LAP contained in the aerosol layer between 450 and 600 meters altitude, as highlighted by the elastic backscattering signal in Fig. 6(b). The effect of the chosen detection wavelength (λ = 633 nm) on the observed LII-vertical profile basically originates from Planck's law, as described by Eq. (4) and as plotted in Fig. 5(c). The extinction of this emitted Planck radiation by other atmospheric compounds, principally water vapor and dioxygen, corresponding to the transmission of the atmosphere appearing in Eq. (4), is negligible at λ = 633 nm along our 600 meters short optical path. The interpretation of the LII-lidar vertical profile remains arguable because the only proof of LAP-presence is given by the range-corrected elastic backscattering signal at λ_L = 532 nm. However, the assumption of LAP-presence appears realistic in the planetary boundary layer of Lyon city, as we published [28].

5. Conclusion and outlooks

In this paper, for the first time to our knowledge, the LII-thermal radiation emitted by light-absorbing-particles (LAP) has been remotely measured, by providing a range-resolved vertical profile of LII-radiation in an urban polluted atmosphere (Lyon, France), over a range of several hundreds of meters. This task is difficult to achieve since the LII-lidar signal can be as low as 100 times lower than the intensity of atmospheric Raman vibrational sidebands, but the range-resolved ability offered by lidar remote sensing may lead to several applications in radiative transfer and climatology. Starting from Kirchhoff's law, we first established the formalism associated with this atmospheric LII-lidar methodology by setting the atmospheric LII-lidar equation and introducing a volume incandescence coefficient β_{LII}, proportional to the soot volume fraction, in analogy with the backscattering coefficient used in the lidar community [20]. For incandescence occurs during a characteristic time τ, the atmospheric LII-lidar equation takes the mathematical form of a convolution product between β_{LII} and the Planck's distribution. To address the main requirements for operating the atmospheric LII-lidar methodology in the low troposphere, we then numerically simulated the LII-lidar equation. It follows that, to observe an LII-lidar signal in the low troposphere, the laser beam divergence should be very low (in the range of 0.05 mrad). Moreover, we proposed a new approach by initiating LII in the IR spectral range and detecting it in the VIS range ($\lambda_L > \lambda$) so as to remove the recorded atmospheric spectrum from both vibrational Raman backscattering sidebands and PAH-fluorescence, even at high quenching rates. Hence, the weak LII-radiation becomes accessible with the state-of-the-art optoelectronics. Two experimental configurations have been proposed for detecting LII in the atmosphere, allowing either spectrally-resolved LII-lidar measurements over a range interval (ICCD gated camera coupled to a Czerny-Turner spectrometer) or range-resolved LII-lidar measurements at a single detection wavelength (1λ-LII-lidar). With the spectrally-resolved LII-lidar detector, we could adjust the recorded atmospheric spectrum with Planck's law, as a clear signature of LII. Then, using the range-resolved LII-lidar detector, we recorded the first vertical profile of LII-radiation in the low troposphere over several hundreds of meters. Interpreting this profile is however not straightforward, as explained in Section 2 by our numerical simulation. In the atmosphere, LAP are not isolated but embedded in ambient air so that sublimation of the adsorbed layer of molecules may eventually occur. To retrieve the LAP-content, a calibration procedure with co-located complementary measurements should then be performed, which is far beyond the scope of this paper. Such co-located measurements could then allow evaluating the sensitivity of our LII-lidar to LAP-detection. Hence, for the atmospheric LII-lidar to provide range-resolved data on the absorptive part of aerosols, to access to the aerosols microphysics, several works must be done to increase the signal-to-noise ratio. This task can be done by taking benefit from the work done in the field of combustion diagnostics [16–18], and

#226547 - $15.00 USD Received 7 Nov 2014; revised 8 Jan 2015; accepted 9 Jan 2015; published 28 Jan 2015

noticeably by acting on the laser fluence. In addition, laboratory experiments and atmospheric measurements must be performed in complement with numerical simulations [25] that now start to have the ability to deal with the complexity of LAP in the atmosphere. Another outlook is relative to the here proposed combination of the LII-lidar with backscattering-lidar, which may then be used to partition refractory particles such as black carbon which may incandesce, from non-refractory particles which are non-incandescent but backscatter laser light. Finally, by initiating LII in the IR spectral range while performing elastic measurements in the VIS spectral range, we emphasized the need for performing 2λ-LII-lidar measurements, which were not feasible at the time of the experiment since both laser sources should alternate. As shown by recent laboratory measurements on 2λ-LII [27], such an approach appears to be very promising, especially when coupled with the range-resolved lidar remote sensing methodology. In addition, a two-color detection would give the opportunity to better constraint the temperature distribution of the emitters.

Acknowledgments

The authors thank Benoit Thuillier for his help in doing the experiments. INERIS and ADEME are thanked for partly funding this work.

#226547 - $15.00 USD Received 7 Nov 2014; revised 8 Jan 2015; accepted 9 Jan 2015; published 28 Jan 2015